


Cite this: *Nanoscale Adv.*, 2022, 4, 600Received 25th October 2021  
Accepted 12th December 2021

DOI: 10.1039/d1na00772f

rsc.li/nanoscale-advances

# FeSi<sub>2</sub>: a two-dimensional ferromagnet containing planar hexacoordinate Fe atoms†

Ying Zhao,<sup>a</sup> Qinxin Liu,<sup>a</sup> Jianpei Xing,<sup>a</sup> Xue Jiang <sup>\*a</sup> and Jijun Zhao<sup>ab</sup>

As an unconventional bonding pattern different from conventional chemistry, the concept of planar hypercoordinate atoms was first proposed in the molecular system, and it has been recently extended to 2D periodic systems. Using first-principles calculations, herein we predict a stable FeSi<sub>2</sub> monolayer with planar hexacoordinate Fe atoms. Due to its abundant multicenter bonds, the FeSi<sub>2</sub> monolayer shows excellent thermal and kinetic stability, anisotropic mechanical properties and room-temperature ferromagnetism ( $T_C \sim 360$  K). Furthermore, we have demonstrated the feasibility of directly growing an FeSi<sub>2</sub> monolayer on a Si (110) substrate while maintaining the novel electronic and magnetic properties of the freestanding monolayer. The FeSi<sub>2</sub> monolayer synthesized in this way would be compatible with the mature silicon semiconductor technology and could be utilized for spintronic devices.

## 1. Introduction

As the core of chemistry, design and synthesis of compounds with novel bonding characteristics have been pursued for decades. In 1970, Hoffmann *et al.* proposed a creative strategy to stabilize planar tetracoordinate carbons through  $\sigma$ -donors and  $\pi$ -acceptors, which violates the classical tetrahedral configuration theory of carbon and leads to the exploration of planar hypercoordinate carbon compounds.<sup>1,2</sup> Discovery of this unique bonding pattern enriches our knowledge of chemical bonds and promotes the exploration of planar hypercoordinate molecules.

Stimulated by the upsurge of 2D materials, there have been some attempts to extend planar hypercoordinate bonding into 2D periodic lattices.<sup>3</sup> To date, plenty of 2D hypercoordinate structures have been predicted, and few of them have been synthesized.<sup>4–7</sup> For example, FeB<sub>2</sub> and CaSi monolayers with planar hexacoordinate Fe and Si atoms, respectively, exhibit excellent electronic and optical properties from theoretical calculations.<sup>8,9</sup> Yang *et al.* proposed a series of nonmagnetic 2D hexacoordinated monolayers, such as Ni<sub>2</sub>Ge, Cu<sub>2</sub>Si, Cu<sub>2</sub>Ge, Cu<sub>2</sub>As, Au and Cu, showing strong chemical bonding and in-plane stiffness.<sup>10–14</sup> Experimentally, Feng *et al.* synthesized a Cu<sub>2</sub>Si monolayer with planar hexacoordinated Cu and Si atoms by directly evaporating Si atoms on single-crystalline Cu (111).<sup>7</sup> Despite the above progress, there are still two issues in

the research of 2D hypercoordinate materials to be solved urgently.

First of all, few efforts have been devoted to the study of the magnetism of 2D hypercoordinate structures as well as its correlation with the unique multicenter bonds. Zhu *et al.* predicted several transition metal carbide (TMC) (TM = Co, Ni, and Cu) monolayers with planar pentacoordinate carbons. The CoC monolayer is antiferromagnetic (AFM), while the NiC monolayer is ferromagnetic (FM). Both of them have large magnetic anisotropy energy (MAE).<sup>15</sup> Tang *et al.* reported a novel planar hypercoordinate boron structure, *i.e.*,  $\alpha$ -FeB<sub>3</sub>, which is a FM metal with a Curie temperature ( $T_C$ ) of 480 K and large vertical magnetic anisotropy.<sup>16</sup>

Another issue is that only a few 2D planar hypercoordinate structures have been synthesized experimentally, hindering their applications in microelectronic devices.<sup>7</sup> So far, a variety of methods have been developed to fabricate 2D materials, including mechanical exfoliation, chemical vapor deposition, and molecular beam epitaxy.<sup>17–20</sup> However, monolayer materials synthesized by these methods need to be transferred to a suitable insulating substrate for application in electronic devices, and such a transfer process inevitably introduces various impurities and defects. Alternatively, directly growing a monolayer on an insulating substrate avoids such a complicated transfer process and prevents the formation of associated defects. Due to their low cost, moderate band gap, and mature technology, silicon substrates are widely used for growing nanomaterials.<sup>21,22</sup>

In this paper, we design a planar FeSi<sub>2</sub> monolayer containing unusual hexacoordinate Fe atoms. The coexistence of delocalized  $\sigma$  bonds and  $\pi$  bonds helps maintain the stability of the monolayer. Remarkably, the FeSi<sub>2</sub> monolayer is a FM metal with a Curie temperature above room temperature. Encouragingly,

<sup>a</sup>Key Laboratory of Materials Modification by Laser, Ion and Electron Beams (Ministry of Education), Dalian University of Technology, Dalian 116024, China. E-mail: jiangx@dlut.edu.cn

<sup>b</sup>Key Laboratory for Intelligent Nano Materials and Devices of the Ministry of Education, Nanjing University of Aeronautics and Astronautics, Nanjing 210016, China

† Electronic supplementary information (ESI) available. See DOI: 10.1039/d1na00772f



the FeSi<sub>2</sub> monolayer can grow directly on a Si (110) substrate, meanwhile retaining its electronic properties and exhibiting enhanced magnetic properties. These results demonstrate that such FM FeSi<sub>2</sub> monolayers may be integrated with silicon-based semiconductor technology, which is conducive to expanding their application in spintronic devices.

## 2. Computational methods

In this work, all calculations were performed using the Vienna *ab initio* simulation package (VASP).<sup>23,24</sup> Ion-electron interactions were described by the projector-augmented plane wave (PAW) approach.<sup>25,26</sup> The generalized gradient approximation (GGA) with the Perdew–Burke–Ernzerhof (PBE) functional was used to describe the exchange–correlation interaction.<sup>27</sup> A plane-wave basis set was adopted with an energy cutoff of 500 eV. The energy precision of self-consistent electronic structure calculations was set to 10<sup>−7</sup> eV, and the atomic position was fully relaxed until the maximum force on each atom was less than 10<sup>−3</sup> eV Å<sup>−1</sup> during optimization. A vacuum space of 20 Å along the perpendicular direction was imposed to avoid interactions between adjacent replicas. The Brillouin zone was sampled with a 19 × 8 × 1 *Γ*-centered Monkhorst–Pack *k*-point grid.<sup>28</sup> To account for the strong correlation effects involving *d* electrons, a Hubbard on-site Coulomb term  $U - J = 3.29$  eV was applied to the Fe atom.<sup>29</sup>

Phonon dispersion of the FeSi<sub>2</sub> monolayer was computed using the direct supercell method implemented in the Phonopy code.<sup>30</sup> To evaluate the thermal stability, *ab initio* molecular dynamics (AIMD) simulations in the *NVT* ensemble was performed with a time step of 1 fs. The initial configurations of the FeSi<sub>2</sub> monolayer in a 6 × 3 × 1 supercell (18 Fe atoms and 36 Si atoms) were kept at different temperatures (300, 600, and 900 K) for 10 ps. The Curie temperature of the FeSi<sub>2</sub> monolayer was evaluated using Monte Carlo simulation with the Wolff algorithm based on the Heisenberg model.<sup>31,32</sup> The Monte Carlo steps were set to 1.2 × 10<sup>5</sup> on a 32 × 32 lattice, and all of the renormalization group Monte Carlo algorithms described here were implemented in the MCSOLVER.<sup>33</sup> The solid-state adaptive natural density partitioning (SSAdNDP) algorithm was used to analyze the chemical bonding pattern of the FeSi<sub>2</sub> monolayer.<sup>34</sup> SSAdNDP is an extension of the AdNDP method in a periodic system and follows the concept of the periodic natural bond orbital method to interpret chemical bonding in terms of classical lone pairs, two-center bonds, and multi-center delocalized bonds.<sup>35,36</sup>

The interface structure can be constructed by stacking the (2 × 3) FeSi<sub>2</sub> monolayer on a five-layer slab model of the (1 × 5) Si (110) surface. The in-plane lattice mismatch between the FeSi<sub>2</sub> monolayer and Si substrate is small, *i.e.* about 3%. The van der Waals (vdW) interaction between the FeSi<sub>2</sub> monolayer and Si substrate was described by Grimme's DFT-D3 scheme.<sup>37</sup> The whole structure was fully relaxed with only the bottom three layers of Si atoms fixed. Charge transfer between the FeSi<sub>2</sub> sheet and Si substrate was evaluated by the Bader charge analysis.<sup>38</sup> To help experimental identification, the constant-current scanning tunneling microscopy (STM) image of the FeSi<sub>2</sub>

monolayer grown on the Si (110) surface was simulated using the Tersoff–Hamann approach implemented in the bSKAN code.<sup>39–41</sup>

## 3. Results and discussion

Inspired by the atomic structure of the 3D bulk  $\alpha$ -FeSi<sub>2</sub> phase, we constructed the FeSi<sub>2</sub> monolayer by considering a one-unit cell along the (110) surface. The FeSi<sub>2</sub> monolayer also belongs to the *Pmmm* crystallographic group (no. 47) with lattice constants of  $a = 2.61$  and  $b = 5.97$  Å.<sup>42</sup> Fig. 1(a) presents the top and side views of the FeSi<sub>2</sub> monolayer, in which each Fe atom coordinates with four Si atoms and two Fe atoms to form a planar hexacoordinate structure with Fe–Si and Fe–Fe bond lengths of 2.25 and 2.62 Å, respectively. To assess the stability of the monolayer structure, we computed the cohesive energy  $E_{\text{coh}}$  defined as:

$$E_{\text{coh}} = (E_{\text{Fe}} + 2E_{\text{Si}} - E_{\text{FeSi}_2})/3, \quad (1)$$

where  $E_{\text{Fe}}$ ,  $E_{\text{Si}}$ , and  $E_{\text{FeSi}_2}$  are the total energies of an individual Fe atom, an individual Si atom, and one unit cell of the FeSi<sub>2</sub> monolayer, respectively. The cohesive energy of the FeSi<sub>2</sub> monolayer is 4.32 eV per atom, which is slightly lower than that of the bulk tetragonal phase of FeSi<sub>2</sub> (5.18 eV per atom) but higher than those of silicene (4.03 eV per atom), germanene (3.30 eV per atom), and Cu<sub>2</sub>Si monolayers (3.65 eV per atom) calculated using the same scheme. We also calculated the formation energy of the FeSi<sub>2</sub> monolayer, which is defined as:

$$E_{\text{f}} = (E_{\text{FeSi}_2} - \mu_{\text{Fe}} - 2\mu_{\text{Si}})/3, \quad (2)$$

where  $\mu_{\text{Fe}}$  and  $\mu_{\text{Si}}$  are the energies of each atom for Fe and Si in their stable bulk phases, respectively. The formation energy is −0.36 eV per atom, corresponding to the exothermic reaction process, which further indicates the possibility of synthesis.

The dynamic stability of the FeSi<sub>2</sub> monolayer was confirmed by the phonon spectrum. As seen in Fig. 1(b), there is no imaginary frequency in the entire Brillouin zone, indicating that the configuration is stable against distortion perturbation. Furthermore, the evolution of total energy and snapshots of the final structures of the FeSi<sub>2</sub> monolayer at different temperatures

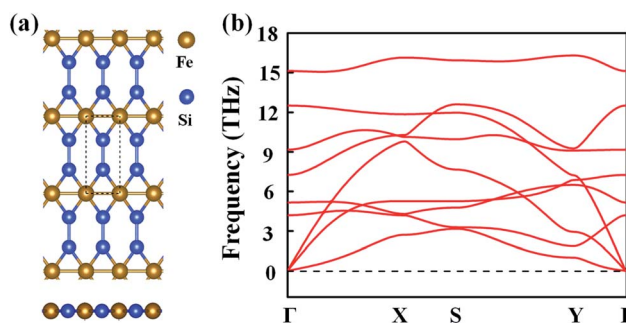


Fig. 1 (a) Top and side views of the FeSi<sub>2</sub> monolayer. The dashed lines represent a unit cell, while  $a$ ,  $b$  and  $c$  represent the lattice vectors. (b) Phonon spectrum of the FeSi<sub>2</sub> monolayer.



from AIMD simulations are shown in Fig. S1.† The framework of the FeSi<sub>2</sub> monolayer is well maintained at 600 K, with the energy fluctuating in a small range (~0.12 eV per atom). These results confirm that the FeSi<sub>2</sub> monolayer has good thermal stability and could be used in devices under high-temperature conditions.

In addition, we calculated the 2D elastic constants of the FeSi<sub>2</sub> monolayer, which are  $C_{11} = 85.72 \text{ N m}^{-1}$ ,  $C_{22} = 154.10 \text{ N m}^{-1}$ ,  $C_{66} = 34.26 \text{ N m}^{-1}$ , and  $C_{12} = C_{21} = 32.02 \text{ N m}^{-1}$ . According to the Born criteria, the mechanical stability of the FeSi<sub>2</sub> monolayer, which belongs to the orthorhombic system, should satisfy  $C_{66} > 0$  and  $C_{11}C_{22} - 2C_{12}^2 > 0$ .<sup>43</sup> Clearly, both criteria are well satisfied, indicating that the FeSi<sub>2</sub> monolayer structure is mechanically stable.

To better describe the type of chemical bonding in the FeSi<sub>2</sub> monolayer, SSAdNDP analyses were performed for a  $3 \times 1 \times 1$  supercell by considering spin polarization, and the results for two spin channels are shown in Fig. 2. For the spin-up states, there are twelve single electrons, three two-center-one-electron (2c-1e)  $\sigma$  bonds, six 3c-1e  $\sigma$  bonds, three 4c-1e  $\sigma$  bonds, and three 7c-1e  $\pi$  bonds. For the spin-down states, there are six single electrons occupying Fe atoms, three 2c-1e  $\sigma$  bonds, six

3c-1e  $\sigma$  bonds, three 4c-1e  $\sigma$  bonds, and three 7c-1e  $\pi$  bonds. These results unveil that the existence of multi-center delocalized bonds and abundant  $\pi$  bonds is helpful to maintain the planar stability of the FeSi<sub>2</sub> monolayer.

To further understand the bonding nature of the FeSi<sub>2</sub> monolayer, we calculated the electron localization function (ELF). As shown in Fig. S2(a),† the ELF isosurface shows substantial accumulation of electrons in the middle of Si-Si bonds, indicating strong covalent interactions in the Si network. In contrast, the Fe atoms are electron deficient with a nearly zero ELF value. Differential charge density and Hirshfeld charge analyses were also performed to reveal the charge transfer behavior between Fe and Si atoms.<sup>44</sup> The differential charge density in Fig. S2(b)† shows that charge transfer occurs from Fe atoms to Si atoms; the charge density is delocalized over the Fe-Si bonds, contributing to the stabilization of the FeSi<sub>2</sub> monolayer. Hirshfeld charge analysis reveals that each Fe atom donates about 0.084 electrons to the adjacent Si atoms. The charge accumulation on Fe-Si bonds and the small amount of charge transfer between Fe atoms and Si atoms indicate covalent interactions between these two types of atoms. As in the cases of Cu<sub>2</sub>Si (~0.06|e|) and FeB<sub>2</sub> (~0.051|e|) monolayer



Fig. 2 SSAdNDP chemical bonding patterns of the FeSi<sub>2</sub> monolayer. ON denotes the occupation number. The yellow and cyan represent positive and negative charge regions, respectively. The results for the spin-up and spin-down states are presented separately.



structures, such a small amount of charge transfer is sufficient to ensure the stability of 2D lattices.<sup>8,10</sup>

Furthermore, we examined the in-plane Young's modulus  $E(\theta)$  and Poisson ratio  $\nu(\theta)$  along any direction  $\theta$  (where  $\theta$  is the angle relative to the positive  $a$  direction), which can be calculated as follows:<sup>45</sup>

$$E(\theta) = \frac{C_{11}C_{22} - C_{12}^2}{C_{11}s^4 + C_{22}c^4 + \left(\frac{C_{11}C_{22} - C_{12}^2}{C_{66}} - 2C_{12}\right)c^2s^2}, \quad (3)$$

$$\nu(\theta) = -\frac{\left(C_{11} + C_{22} - \frac{C_{11}C_{22} - C_{12}^2}{C_{66}}\right)c^2s^2 - C_{12}(c^4 + s^4)}{C_{11}s^4 + C_{22}c^4 + \left(\frac{C_{11}C_{22} - C_{12}^2}{C_{66}} - 2C_{12}\right)c^2s^2}, \quad (4)$$

where  $c = \cos \theta$ , and  $s = \sin \theta$ . The calculated  $E(\theta)$  and  $\nu(\theta)$  values in Fig. S3† indicate that the Young's modulus in the  $b$  direction has a maximum value of  $142 \text{ N m}^{-1}$ , which is approximately two times larger than that in the  $a$  direction. This value is smaller than that of graphene ( $341 \text{ N m}^{-1}$ ), but larger than that of the  $\text{Cu}_2\text{Si}$  monolayer ( $93 \text{ N m}^{-1}$ ) and the  $\text{MoS}_2$  monolayer ( $129 \text{ N m}^{-1}$ ).<sup>7,46,47</sup> The Poisson ratio is also anisotropic with a maximum value of 0.37 along the  $a$  direction and a minimum value of 0.21 along the  $b$  direction. The prominent anisotropy in both the Young's modulus and Poisson ratio implies that the  $\text{FeSi}_2$  monolayer may have intriguing mechanical applications.

Next, we discuss the electronic properties of the  $\text{FeSi}_2$  monolayer. The spin-polarized band structures are displayed in Fig. 3(a). Several bands in both spin-up and spin-down channels cross the Fermi level; thus, the  $\text{FeSi}_2$  monolayer is metallic. We also employ the Heyd–Scouseria–Ernzerhof (HSE06) functional to further confirm its band characteristics. As shown in Fig. S4,† the  $\text{FeSi}_2$  monolayer still exhibits a metallic nature. As revealed by the partial density of states (PDOS) of the  $\text{FeSi}_2$  monolayer in Fig. 3(b), the density of states at the Fermi level is mainly contributed by Fe 3d orbitals.

The calculated spin polarization of electrons in Fig. 4(a) indicates that the magnetism mainly originates from Fe with a magnetic moment of  $2.27 \mu_{\text{B}}$  per Fe atom, which can be explained within the framework of crystal field theory [see Fig. 4(b)]. Due to symmetry breaking under the planar hexagonal crystal field, the five degenerate d orbitals of the Fe atom split into three groups: the degenerate  $d_{xy}$  and  $d_{x^2-y^2}$  orbitals with higher energy, the  $d_{z^2}$  orbital with intermediate energy, and the degenerate  $d_{yz}$  and  $d_{zx}$  orbitals with lower energy. In the  $\text{FeSi}_2$  monolayer, distortion of the hexagonal plane leads to further splitting of the orbitals so that the five d orbitals are no longer degenerate. According to the above bonding analysis, although there is a small amount of charge transfer between the Fe and Si atoms, the total number of valence electrons on the Fe atom ( $[\text{Ar}]3d^74s^1$ ) remains nearly intact. Because of the competition between the Coulomb repulsion and the crystal field splitting energy, electrons will first occupy the orbitals with parallel spin according to Hund's rule. Finally, all five spin-up d orbitals are occupied, while the spin-down  $d_{xz}$  and  $d_{z^2}$  orbitals are left empty. Hence, the spin magnetic moment on each Fe atom should be approximately  $2.0 \mu_{\text{B}}$ , consistent with the PDOS picture for the Fe atom from DFT calculations [Fig. 4(c)]. The above SSAdNDP analysis shows that in the  $3 \times 1 \times 1$  supercell, the spin-up states of six 1c–1e bonds on Fe atoms are unpaired, resulting in the spin polarization of the system. In the supercell, the difference between the numbers of occupied spin-up and spin-down states from the SSAdNDP analysis is about  $6.53|e|$ , which is almost the same as the calculated magnetic moment of  $\sim 6.34 \mu_{\text{B}}$ .

The magnetic ground state of the  $\text{FeSi}_2$  monolayer was determined by comparing the energy of the FM state with those of seven AFM configurations shown in Fig. S5.† The energy differences of different AFM configurations relative to the FM state are listed in Table S1,† demonstrating that the ground state is FM. Also note that the magnetic moment and magnetic ground state are not affected by the HSE06 functional. In order to understand the magnetic exchange mechanism in the  $\text{FeSi}_2$

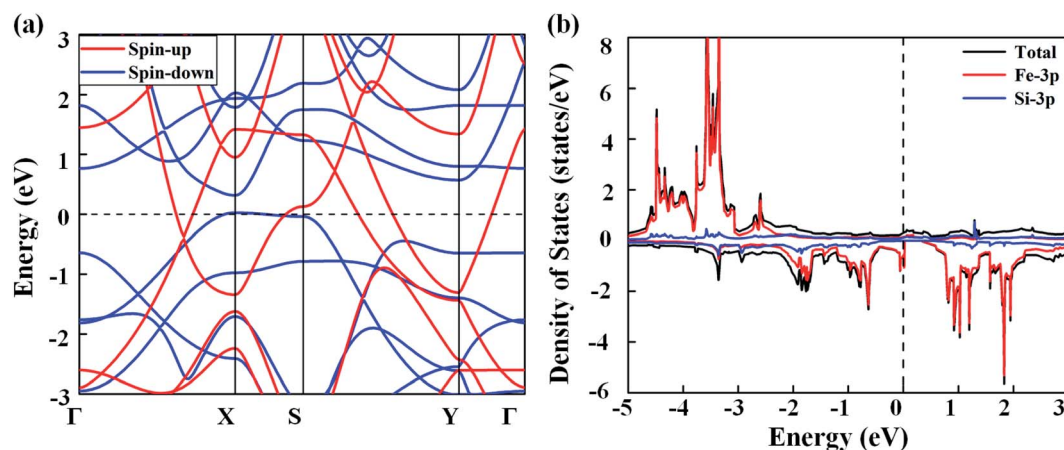


Fig. 3 (a) Spin-polarized band structures of the  $\text{FeSi}_2$  monolayer. (b) Total and partial density of states of the  $\text{FeSi}_2$  monolayer. The Fermi level (dashed line) is set to zero.



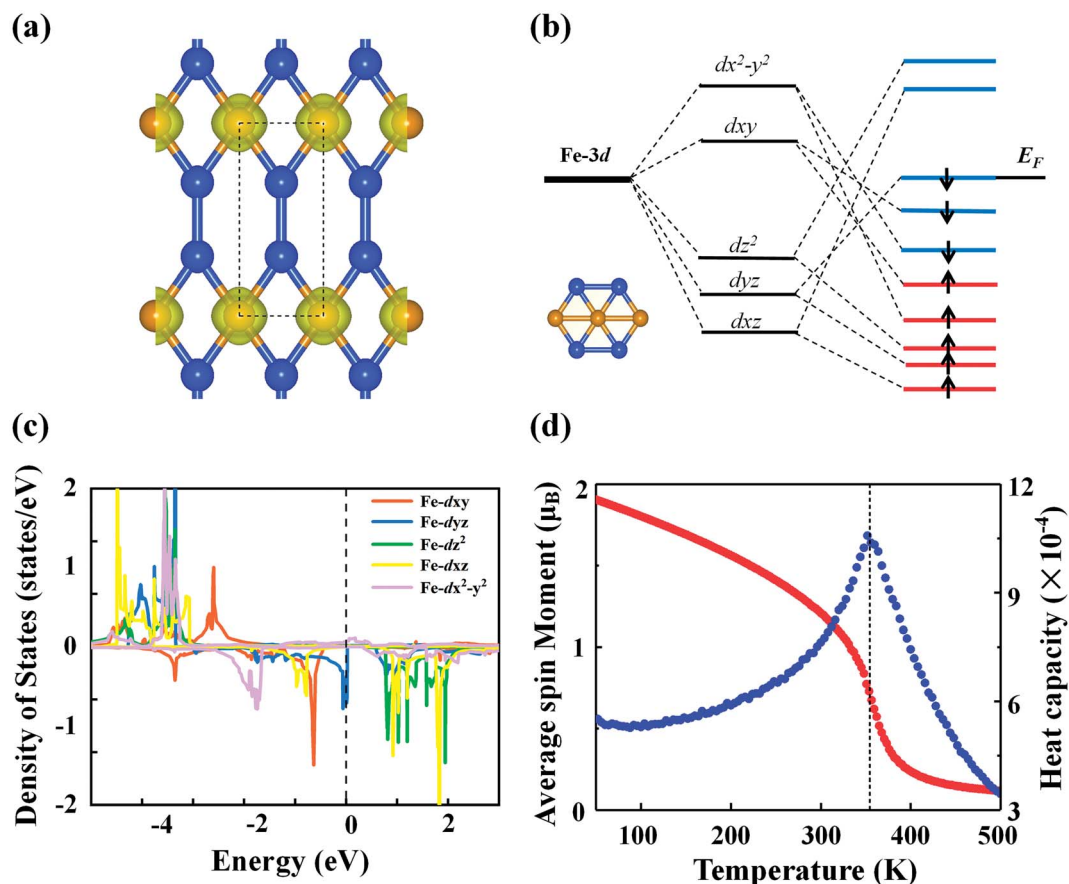


Fig. 4 (a) Spin density distributions of the FeSi<sub>2</sub> monolayer with an isosurface of 0.015 au. The dashed lines represent a unit cell. (b) Splitting of the d orbitals of the Fe atom in the crystal field. The inset is a schematic structure of the distorted hexagonal plane in the FeSi<sub>2</sub> monolayer. (c) Partial orbital density of states of the Fe atom in the FeSi<sub>2</sub> monolayer. (d) Average magnetic moment per Fe atom (red scatter) and heat capacity (blue scatter) of the FeSi<sub>2</sub> monolayer as a function of temperature from Monte Carlo simulations.

monolayer, we considered seven-order spin-exchange interaction (Fig. S5<sup>†</sup>) to ensure that the exchange parameter  $J_i$  can converge to a small value. The exchange parameter  $J_i$  and the corresponding Fe–Fe distance  $d_i$  are listed in Table S2.<sup>†</sup> As the distance between the magnetic atoms increases, the exchange parameter  $J_i$  does not decrease consistently; instead,  $J_i$  oscillates with an overall decreasing trend. This suggests that the magnetic exchange mechanism in the FeSi<sub>2</sub> monolayer belongs to the indirect Ruderman–Kittel–Kasuya–Yosida (RKKY) interaction, similar to that of the planar hypercoordinate FeB<sub>3</sub> monolayer reported before.<sup>16</sup> Using the exchange parameter  $J_i$ , we performed Monte Carlo (MC) simulation based on the 2D Heisenberg model to estimate the Curie temperature of the FeSi<sub>2</sub> monolayer. The Curie temperature [Fig. 4(d)] is approximately 360 K, which is above room temperature and higher than those of 2D planar FM monolayers of  $\chi_3$  CrB<sub>4</sub> (242 K) and orthorhombic phase FeC<sub>2</sub> (245 K), both belonging to 2D hypercoordinate compounds by transition metals and light nonmetal elements.<sup>48,49</sup> Taking spin–orbit coupling into account, we further compared the energies of the FeSi<sub>2</sub> monolayer among four magnetization directions, namely, (100), (010), (110), and (001). The easy magnetization axis is along the (100) direction with a MAE of 56  $\mu$ eV per Fe atom.

With all these unique chemical and physical properties, we expect to prepare this FeSi<sub>2</sub> monolayer experimentally. Since its 3D FeSi<sub>2</sub> parent is a non-vdW layered material, it is difficult to obtain a FeSi<sub>2</sub> monolayer by mechanical exfoliation. However, such a 2D non-vdW material may synthesize directly on a suitable substrate by the molecular beam epitaxy (MBE) or chemical vapor deposition (CVD) method. Based on the two methods, several 2D non-vdW ultrathin films have been recently synthesized successfully.<sup>50,51</sup> Among the low-index Si surfaces, the Si (110) surface has been widely used in the synthesis of electronic devices, and the Si (110) surface also has higher hole mobility than the other surfaces.<sup>52–54</sup> Upon using our structural model of the (2 × 3) FeSi<sub>2</sub> monolayer on the (1 × 5) Si (110) surface, the lattice mismatch is less than 3% upon relaxation. In order to accommodate the strain energy caused by lattice mismatch, the Fe–Si bond length in the heterostructure changes and the Si-supported FeSi<sub>2</sub> layer is slightly distorted compared to the freestanding monolayer [Fig. 5(a)]. The interlayer distance between the FeSi<sub>2</sub> monolayer and Si (110) surface is about 2.28 Å. Specifically, the average distance between Fe atoms and substrate Si atoms is about 2.64 Å, which is comparable to the covalent Fe–Si bond length (2.40 Å) in the freestanding FeSi<sub>2</sub> monolayer.



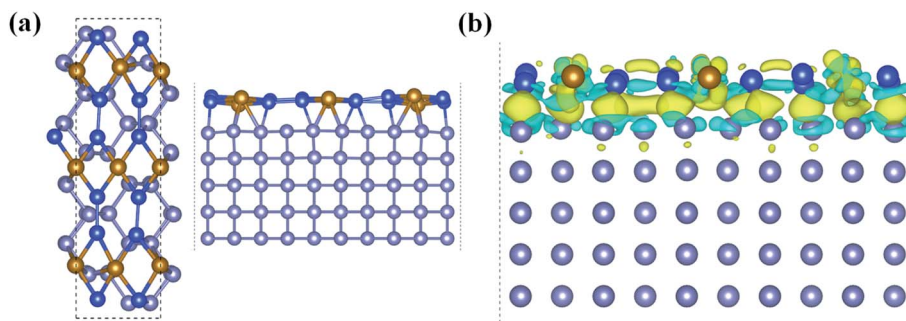


Fig. 5 (a) Top and side views of the FeSi<sub>2</sub> monolayer on the Si (110) substrate. (b) Differential charge density between the FeSi<sub>2</sub> monolayer and the Si (110) surface, with an isosurface value of  $4 \times 10^{-3} \text{ e} \times \text{\AA}^{-3}$ . The yellow and cyan regions represent electron accumulation and depletion, respectively.

To describe the interfacial interaction between the FeSi<sub>2</sub> monolayer and Si (110) substrate, we calculated the formation energy defined as:

$$E_f = (E_{\text{tot}} - E_{\text{FeSi}_2} - E_{\text{sub}})/N_{\text{atom}}, \quad (5)$$

where  $E_{\text{FeSi}_2}$ ,  $E_{\text{sub}}$  and  $E_{\text{tot}}$  denote the total energies of the FeSi<sub>2</sub> monolayer, Si (110) substrate, and FeSi<sub>2</sub>/Si (110) heterostructure, respectively;  $N_{\text{atom}}$  is the number of atoms in the FeSi<sub>2</sub> monolayer. The calculated formation energy is  $-0.81 \text{ eV}$  per atom, which is stronger than those of silicene/Ag (111) ( $-0.67 \text{ eV}$  per atom) and c-BSi<sub>3</sub>/Ag (111) ( $-0.54 \text{ eV}$  per atom) heterojunctions.<sup>55,56</sup> The negative formation energy indicates that the heterostructure is energetically favorable and easy to obtain.

In addition, we plotted the differential charge density to visually show the interface interaction between the monolayer and substrate, as shown in Fig. 5(b). Obviously, due to the strong interface interaction between the FeSi<sub>2</sub> monolayer and Si (110) surface, the charge is redistributed near the interface, which is conducive to interface adhesion, suggesting that the FeSi<sub>2</sub> monolayer can be grown directly on the Si (110) substrate. The method of preparing a 2D thin film by using the strong interaction between the film and substrate has been widely used in experiments.<sup>57–61</sup> For future experimental identification, we also simulated the STM image of the FeSi<sub>2</sub> monolayer on the Si (110) surface. The bright areas in the simulated STM image are associated with Fe atoms (see the labels in Fig. S6†).

We also examined the effects of the substrate on the electronic and magnetic properties of the FeSi<sub>2</sub> monolayer. As shown in Fig. S7,† compared with the freestanding FeSi<sub>2</sub> monolayer without the Si (110) substrate, the DOS peak of the freestanding FeSi<sub>2</sub> monolayer with the substrate becomes flatter and the peak decreases, which may be due to the formation of chemical bonds by charge transfer between the FeSi<sub>2</sub> monolayer and substrate. The energy differences between the FM and AFM states (Table S2†) indicate that the magnetic ground state of the FeSi<sub>2</sub> monolayer on the silicon substrate remains in the FM state. In comparison to the case of the freestanding monolayer, the MAE and average magnetic moment of the FeSi<sub>2</sub> monolayer on the silicon substrate are enhanced to  $1.34 \text{ meV}$  per Fe atom and  $2.87 \mu_B$  per Fe atom, respectively, and the easy

magnetization axis remains in the in-plane direction. These findings indicate that the Si (110) substrate not only provides a structural template for the deposited FeSi<sub>2</sub> film but the interaction between the film and the substrate itself leads to enhanced magnetic properties.

## 4. Conclusions

In summary, we designed a new stable planar hexacoordinate 2D FeSi<sub>2</sub> monolayer in which each Fe atom is coordinated to four Si atoms and two adjacent Fe atoms. Based on first-principles calculations, we comprehensively explored the mechanical, electronic, and magnetic properties of the FeSi<sub>2</sub> monolayer. The results revealed that the monolayer has in-plane mechanical anisotropy and high stability due to abundant multicenter bonds. Notably, the FeSi<sub>2</sub> monolayer exhibits strong intrinsic ferromagnetism with a high  $T_C$  ( $\sim 360 \text{ K}$ ). The robust magnetic coupling can be attributed to the indirect RKKY interaction. Furthermore, we predicted that the FeSi<sub>2</sub> monolayer can grow directly on the insulating Si (110) substrate, meanwhile the magnetic moment and MAE can be significantly improved. Our findings enrich the diversity of planar hypercoordinate transition metal compounds, and the attractive properties revealed in this study make the FeSi<sub>2</sub> monolayer a promising candidate for applications in spintronics.

## Conflicts of interest

There are no conflicts to declare.

## Acknowledgements

This work was supported by the Genetic Engineering of Precious Metal Materials in Yunnan Province (I)-Construction and Application of Precious Metal Materials Professional Database (I) (202002AB080001-1), Science Challenge Project (TZ2018004) and National Natural Science Foundation of China (11874097). We acknowledge the Xinghai Scholar project of Dalian University of Technology. The authors also acknowledge the Supercomputing Center of Dalian University of Technology for providing the computing resources.



## References

- R. Hoffmann, R. W. Alder and C. F. Wilcox Jr, *J. Am. Chem. Soc.*, 1970, **92**, 4992–4993.
- J. A. Le Bel, *Bull. Soc. Chim. Fr.*, 1874, **22**, 337–347.
- Y. Wang, Y. Li and Z. Chen, *Acc. Chem. Res.*, 2020, **53**, 887–895.
- C.-S. Liu, H.-H. Zhu, X.-J. Ye and X.-H. Yan, *Nanoscale*, 2017, **9**, 5854–5858.
- X. Qu, J. Yang, Y. Wang, J. Lv, Z. Chen and Y. Ma, *Nanoscale*, 2017, **9**, 17983–17990.
- H. Zhang, Y. Li, J. Hou, K. Tu and Z. Chen, *J. Am. Chem. Soc.*, 2016, **138**, 5644–5651.
- B. Feng, B. Fu, S. Kasamatsu, S. Ito, P. Cheng, C.-C. Liu, Y. Feng, S. Wu, S. K. Mahatha, P. Sheverdyeva, P. Moras, M. Arita, O. Sugino, T.-C. Chiang, K. Shimada, K. Miyamoto, T. Okuda, K. Wu, L. Chen, Y. Yao and I. Matsuda, *Nat. Commun.*, 2017, **8**, 1007.
- H. Zhang, Y. Li, J. Hou, A. Du and Z. Chen, *Nano Lett.*, 2016, **16**, 6124–6129.
- Y. Wang, M. Qiao, Y. Li and Z. Chen, *Nanoscale Horiz.*, 2018, **3**, 327–334.
- L.-M. Yang, V. Bačić, I. A. Popov, A. I. Boldyrev, T. Heine, T. Frauenheim and E. Ganz, *J. Am. Chem. Soc.*, 2015, **137**, 2757–2762.
- L.-M. Yang, M. Dornfeld, T. Frauenheim and E. Ganz, *Phys. Chem. Chem. Phys.*, 2015, **17**, 26036–26042.
- L.-M. Yang, T. Frauenheim and E. Ganz, *J. Nanomater.*, 2016, 2016.
- L.-M. Yang and E. Ganz, *Phys. Chem. Chem. Phys.*, 2016, **18**, 17586–17591.
- L.-M. Yang, I. A. Popov, A. I. Boldyrev, T. Heine, T. Frauenheim and E. Ganz, *Phys. Chem. Chem. Phys.*, 2015, **17**, 17545–17551.
- C. Zhu, H. Lv, X. Qu, M. Zhang, J. Wang, S. Wen, Q. Li, Y. Geng, Z. Su, X. Wu, Y. Li and Y. Ma, *J. Mater. Chem. C*, 2019, **7**, 6406–6413.
- C. Tang, K. Ostrikov, S. Sanvito and A. Du, *Nanoscale Horiz.*, 2021, **6**, 43–48.
- K. S. Novoselov, A. K. Geim, S. V. Morozov, D. Jiang, Y. Zhang, S. V. Dubonos, I. V. Grigorieva and A. A. Firsov, *Science*, 2004, **306**, 666–669.
- M. P. Warusawithana, C. Cen, C. R. Slesman, J. C. Woicik, Y. L. Li, L. F. Kourkoutis, J. A. Klug, H. Li, P. Ryan, L. P. Wang, M. Bedzyk, D. A. Muller, L. Q. Chen, J. Levy and D. G. Schlom, *Science*, 2009, **324**, 367–370.
- J. Jeon, S. K. Jang, S. M. Jeon, G. Yoo, Y. H. Jang, J.-H. Park and S. Lee, *Nanoscale*, 2015, **7**, 1688–1695.
- N. Mounet, M. Gibertini, P. Schwaller, D. Campi, A. Merkys, A. Marrazzo, T. Sohler, I. E. Castelli, A. Cepellotti, G. Pizzi and N. Marzari, *Nat. Nanotechnol.*, 2018, **13**, 246–252.
- W. Heywang and K. H. Zaininger, in *Silicon*, Springer, 2004, pp. 25–42.
- T. Mårtensson, C. P. T. Svensson, B. A. Wacaser, M. W. Larsson, W. Seifert, K. Deppert, A. Gustafsson, L. R. Wallenberg and L. Samuelson, *Nano Lett.*, 2004, **4**, 1987–1990.
- G. Kresse and J. Hafner, *Phys. Rev. B: Condens. Matter Mater. Phys.*, 1993, **47**, 558–561.
- J. Hafner, *J. Comput. Chem.*, 2008, **29**, 2044–2078.
- P. E. Blöchl, *Phys. Rev. B: Condens. Matter Mater. Phys.*, 1994, **50**, 17953.
- G. Kresse and D. Joubert, *Phys. Rev. B*, 1999, **59**, 1758–1775.
- J. P. Perdew, K. Burke and M. Ernzerhof, *Phys. Rev. Lett.*, 1996, **77**, 3865–3868.
- H. J. Monkhorst and J. D. Pack, *Phys. Rev. B: Solid State*, 1976, **13**, 5188–5192.
- S. Iv, P. H. Dederichs and A. Vi, *Phys. Rev. B: Condens. Matter Mater. Phys.*, 1994, **50**, 16861–16871.
- A. Togo, F. Oba and I. Tanaka, *Phys. Rev. B: Condens. Matter Mater. Phys.*, 2008, **78**, 134106.
- M. Lan, G. Xiang, Y. Nie, D. Yang and X. Zhang, *RSC Adv.*, 2016, **6**, 31758–31761.
- M. Kan, J. Zhou, Q. Sun, Y. Kawazoe and P. Jena, *J. Phys. Chem. Lett.*, 2013, **4**, 3382–3386.
- L. Liu, S. Chen, Z. Lin and X. Zhang, *J. Phys. Chem. Lett.*, 2020, **11**, 7893–7900.
- T. R. Galeev, B. D. Dunnington, J. R. Schmidt and A. I. Boldyrev, *Phys. Chem. Chem. Phys.*, 2013, **15**, 5022–5029.
- E. D. Glendening, C. R. Landis and F. Weinhold, *Wiley Interdiscip. Rev.: Comput. Mol. Sci.*, 2012, **2**, 1–42.
- D. Y. Zubarev and A. I. Boldyrev, *Phys. Chem. Chem. Phys.*, 2008, **10**, 5207–5217.
- S. Grimme, S. Ehrlich and L. Goerigk, *J. Comput. Chem.*, 2011, **32**, 1456–1465.
- G. Henkelman, A. Arnaldsson and H. Jónsson, *Comput. Mater. Sci.*, 2006, **36**, 354–360.
- J. Tersoff and D. R. Hamann, *Phys. Rev. Lett.*, 1983, **50**, 1998–2001.
- J. Tersoff and D. R. Hamann, *Phys. Rev. B: Condens. Matter Mater. Phys.*, 1985, **31**, 805–813.
- K. Palotas and W. A. Hofer, *J. Phys.: Condens. Matter*, 2005, **17**, 2705–2713.
- C. Kloc, E. Arushanov, M. Wendl, H. Hohl, U. Malang and E. Bucher, *J. Alloys Compd.*, 1995, **219**, 93–96.
- J. Wang, S. Yip, S. R. Phillpot and D. Wolf, *Phys. Rev. Lett.*, 1993, **71**, 4182–4185.
- P. Bultinck, C. Van Alsenoy, P. W. Ayers and R. Carbó-Dorca, *J. Phys. Chem. C*, 2007, **126**, 144111.
- E. Cadelano, P. L. Palla, S. Giordano and L. Colombo, *Phys. Rev. B: Condens. Matter Mater. Phys.*, 2010, **82**, 235414.
- R. C. Cooper, C. Lee, C. A. Marianetti, X. Wei, J. Hone and J. W. Kysar, *Phys. Rev. B: Condens. Matter Mater. Phys.*, 2013, **87**, 035423.
- C. Lee, X. Wei, J. W. Kysar and J. Hone, *Science*, 2008, **321**, 385.
- X. Li, X. Li and J. Yang, *J. Phys. Chem. Lett.*, 2019, **10**, 4417–4421.
- T. Zhao, J. Zhou, Q. Wang, Y. Kawazoe and P. Jena, *ACS Appl. Mater. Interfaces*, 2016, **8**, 26207–26212.
- L. Kang, C. Ye, X. Zhao, X. Zhou, J. Hu, Q. Li, D. Liu, C. M. Das, J. Yang and D. Hu, *Nat. Commun.*, 2020, **11**, 1–9.



- 51 A. Roy, S. Guchhait, R. Dey, T. Pramanik, C.-C. Hsieh, A. Rai and S. K. Banerjee, *ACS Nano*, 2015, **9**, 3772–3779.
- 52 W. Cheng, A. Teramoto, M. Hirayama, S. Sugawa and T. Ohmi, *Jpn. J. Appl. Phys.*, 2006, **45**, 3110.
- 53 F. Ruiz-Zepeda, O. Contreras, A. Dadgar and A. Krost, *Appl. Phys. Lett.*, 2010, **96**, 231908.
- 54 T. Satô, Y. Takeishi, H. Hara and Y. Okamoto, *Phys. Rev. B: Solid State*, 1971, **4**, 1950–1960.
- 55 N. Gao, H. Liu, S. Zhou, Y. Bai and J. Zhao, *J. Phys. Chem. C*, 2017, **121**, 5123–5129.
- 56 X. Tan, F. Li and Z. Chen, *J. Phys. Chem. C*, 2014, **118**, 25825–25835.
- 57 W. Chang, S. Rajan, B. Peng, C. Ren, M. Sutton and C. Li, *Carbon*, 2019, **153**, 699–706.
- 58 L. Ding, W. Zhou, T. P. McNicholas, J. Wang, H. Chu, Y. Li and J. Liu, *Nano Res.*, 2009, **2**, 903–910.
- 59 M. Velicky, A. Rodriguez, M. Bousa, A. V. Krayev, M. Vondracek, J. Honolka, M. Ahmadi, G. E. Donnelly, F. Huang, H. D. Abruna, K. S. Novoselov and O. Frank, *J. Phys. Chem. Lett.*, 2020, **11**, 6112–6118.
- 60 S. Wang, X. Wang and J. H. Warner, *ACS Nano*, 2015, **9**, 5246–5254.
- 61 X. H. Ye, F. Yu, M. Curioni, Z. Lin, H. J. Zhang, H. W. Zhu, Z. Liu and M. L. Zhong, *RSC Adv.*, 2015, **5**, 35384–35390.

